Inorganic Chemistry

pubs.acs.org/IC

Article

Exfoliable Transition Metal Chalcogenide Semiconductor $NbSe_2I_2$

Kejian Qu, Yue Zhang, Cheng Peng, Zachary W. Riedel, Juyeon Won, Rong Zhang, Toby J. Woods, Tom Devereaux, Arend M. van der Zande, and Daniel P. Shoemaker*

Cite This: *Inorg. Chem.* 2024, 63, 1119−1126

Read Online

ACCESS | Metrics & More | Article Recommendations | Supporting Information

ABSTRACT: As the field of exfoliated van der Waals electronics grows to include complex heterostructures, the variety of available in-plane symmetries and geometries becomes increasingly valuable. In this work, we present an efficient chemical vapor transport synthesis of $NbSe_2I_2$ with the triclinic space group $P\bar{1}$. This material contains Nb−Nb dimers and an in-plane crystallographic angle $\gamma = 61.3°$. We show that $NbSe_2I_2$ can be exfoliated down to few-layer and monolayer structures and use Raman spectroscopy to test the preservation of the crystal structure of exfoliated thin films. The crystal structure was verified by single-crystal and powder X-ray diffraction methods. Density functional theory calculations show triclinic $NbSe_2I_2$ to be a semiconductor with a band gap of around 1 eV, with similar band structure features for bulk and monolayer crystals. The physical properties of $NbSe_2I_2$ have been characterized by transport, thermal, optical, and magnetic measurements, demonstrating triclinic $NbSe_2I_2$ to be a diamagnetic semiconductor that does not exhibit any phase transformation below room temperature.

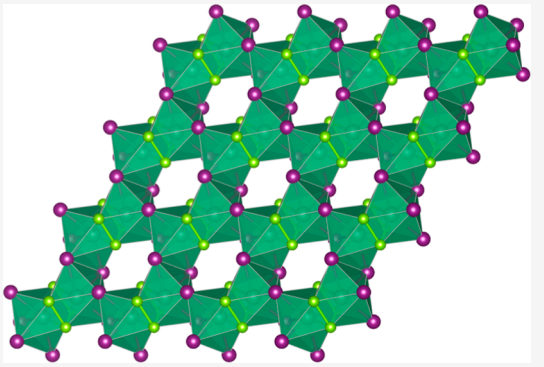

INTRODUCTION

Since the discovery of monolayer graphene in 2004,[1,2] the door for the new families of exfoliable materials has been opened, and the number of two-dimensional (2D) materials as well as the attention they draw has seen exponential growth.[3,4] Materials that consist of 2D layers bonded by van der Waals forces are of particular interest due to the wide variety of complex electronic and spintronic phenomena that can be engineered in thin-film devices. Graphene[5,6] and hexagonal boron nitride (h-BN)[7,8] are canonical examples. More recently, transition metal dichalcogenides (TMDCs)[9,10] such as MoS_2[11] and WTe_2[12] have come under intense studies because of their shallow band gaps compared to the pure metallic behavior of graphene. These TMDCs may host topological behavior[13] with the presence of strong spin−orbit coupling due to the existence of 4d or 5d transition metal elements. Many 2D transition metal chalcogenides have been discovered, including the ternary MPX_3 compounds,[14] where M is a transition metal and X is a chalcogen ion. These materials are widely utilized for their magnetic properties[15,16] due to the well-defined magnetic moment of 3d transition metal ions such as Mn^{2+} and Fe^{2+}.

A chemically related but functionally distinct group of compounds are the ternary transition metal chalcogenide halides,[17] such as $(TaSe_4)_2I$[18,19] and $(NbSe_4)_{3.33}I$,[20] both of which host charge density wave (CDW) behavior. The halides are quasi-one-dimensional materials with parallel $(TaSe_4)_n$ or $(NbSe_4)_n$ chains intercalated by iodine ions, further pushing down the dimensionality. Ta and Nb ions have alternating 4+ and 5+ valence, thus leaving the $(TaSe_4)_n$ or $(NbSe_4)_n$ chains with partially filled conducting d bands and resulting in semiconducting behavior with shallow band gaps, which can possibly be tuned.

There are many ways to synthesize these 2D materials,[21] including liquid exfoliation,[22] chemical vapor deposition,[23] and molecular beam epitaxy.[24] A particularly versatile synthesis method that does not require a substrate is chemical vapor transport (CVT).[25] CVT utilizes a reversible chemical reaction that slowly deposits the target material as single crystals at a temperature that favors solid deposition. For many 2D materials, large crystals were first grown by CVT, such as CrAs[26] and $TaSe_2$,[27] and it is a viable method to discover new materials due to the straightforward setup and the large number of tunable experimental variables. Iodine is the most widely used transport agent, in addition to a large library of possible transport agents,[28] and this will especially lead to the discovery of new iodine-containing compounds.[29] The crystals synthesized by CVT are bulky, but often they can be exfoliated down to a few layers or monolayers if the planes are separated by van der Waals interactions.

Received: October 6, 2023
Revised: December 20, 2023
Accepted: December 21, 2023
Published: January 4, 2024

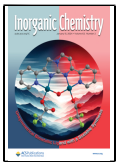

Recently, pristine graphene came back under the spotlight after breakthrough studies on twisted bilayer graphene (TBG) in 2018.[30,31] It has been shown that two graphene layers twisted by a "magic angle" of around 1.1° can exhibit superconductivity or insulating behavior. These studies, together with the earlier studies on single-layer graphene on hBN substrates,[32−34] show that superlattices created from the Moiré effect can intensely control the electronic properties of the heterostructures. The Moiré effect can be caused by twisting angles, as in the case of TBG, or a lattice mismatch, as in the case of graphene on hBN. The plane hexagonal lattice is very common among 2D materials; thus, an exfoliable material with the in-plane crystallographic angle close to, but not exactly, 60° would be a great candidate for exotic Moiré effects.

Here, we show how CVT reactions produce compounds in the Nb−Se−I ternary system,[35] and we present an exfoliable two-dimensional compound $NbSe_2I_2$, which has the space group of $P\bar{1}$ at room temperature,[36,37] with an in-plane crystallographic angle $\gamma = 61.3°$. First, an efficient synthesis of $NbSe_2I_2$ by CVT is reported. Next, the exfoliation of $NbSe_2I_2$ down to few-layer and monolayer structures is shown, and Raman spectroscopy was utilized to study the difference between bulk, few-layer, and monolayer $NbSe_2I_2$ structures. The electronic band structure calculated by density functional theory (DFT), together with transport, thermal, optical, and magnetic measurements, unveils the property of the exfoliable transition metal chalcogenide $NbSe_2I_2$.

METHODS

Synthesis. The CVT synthesis of $NbSe_2I_2$ gained its insight from the CVT synthesis of $(TaSe_4)_2I$[38] as well as the discovery of $(Nb_4Se_{15}I_2)I_2$.[29] Thin sheets of $NbSe_2I_2$ crystals were first discovered from a trial CVT synthesis with the starting ingredients at 460 °C and the crystals grown at a lower temperature of 420 °C. This unusual CVT growth from higher temperature to lower temperature matched with the published synthesis of many Nb−Se−I ternary compounds.[35] However, very few $NbSe_2I_2$ crystals were obtained, mixing with other compounds, likely the binary compound between selenium and iodine, and they were all smaller than 1 × 1 mm. Moreover, we found that this synthesis was not easily reproducible and that $(NbSe_4)_3I$ crystals occasionally grew instead of $NbSe_2I_2$ crystals.

Here, we report an improved synthesis method that produces large (around 2 × 2 mm) and abundant $NbSe_2I_2$ crystals, and the crystals can be easily isolated from byproducts. Similar to the synthesis of $(Nb_4Se_{15}I_2)I_2$, the synthesis of $NbSe_2I_2$ is also highly dependent on sample mass, stoichiometry, form (powder or wire) of ingredients, temperature profile, etc.

The starting ingredients were the same as those for the synthesis of $(Nb_4Se_{15}I_2)I_2$.[29] Elements were ground in an agate mortar with a molar ratio of Nb (99.8%, powder):Se (99.999%, ground shots):I (99.8%, crystalline solid) = 2:8:10.3. The excess 0.3 ratio of iodine was intentionally added to compensate for the loss from sublimation, and the ratio of iodine was larger than any known Nb−Se−I ternary compounds to ensure enough iodine was available to act as the transport agent. The total sample mass was about 0.9 g. After being fully ground with a pestle, the mixture tended to form a porous, loosely bound agglomerate, and Nb powder did not stick to the surface of the mortar.

The powder mixture was loaded into a small fused quartz tube (9 mm outer diameter and 7 mm inner diameter) with one end always open. Next, the small tube was loaded into a larger fused quartz tube (12 mm outer diameter and 10 mm inner diameter). The large tube was then sealed under vacuum, and the smaller tube was situated so that the reagents lay near the middle of the larger tube. We used an inner tube in an attempt to physically separate the nucleation location of the transported product together with the vapor from the reagent by providing easy nucleation spots for $(Nb_4Se_{15}I_2)I_2$, which grew in the mid-lower temperature region (Figure S1). The double-tube assembly was heated in a horizontal two-zone furnace with high- and low-temperature sides at 480 and 280 °C, respectively, with the starting ingredients at around 420 °C. The furnace was programmed so that both sides reached their temperature set points simultaneously after 10 h, and the assembly was held for 80 h before cooling naturally. Figure S1 in Supporting Information[39] shows the reaction tube before and after the reaction.

After the reaction, dozens of single crystals in the form of thin sheets were formed at the same location where the ingredients started. These crystals were mixed with some $(NbSe_4)_3I$ powder byproducts, and the crystals can be easily picked out. The typical dimensions of these crystals can reach 2 × 2 × 0.1 mm. Additionally, a large number of $(Nb_4Se_{15}I_2)I_2$ single crystals were also formed close to the opening of the smaller tube in the temperature range of around 350−300 °C, matching the previously reported temperature range.[29] The "empty" high-temperature portion of the larger tube contained some residual iodine after the reaction. A traditional single-tube CVT synthesis with starting materials at 430 °C and low temperature at 300 °C was also attempted, but $NbSe_2I_2$ crystals did not form and only $(NbSe_4)_3I$ powder was left at the high-temperature side.

$NbSe_2I_2$ crystals were stable when left in the air for several days, but over a longer period of time, the surface tended to degrade and became less shiny.

Structure Determination. We collected single-crystal X-ray diffraction data on a Bruker D8 Venture Duo diffractometer at 299 K and applied an absorption correction using Bruker SADABS. We then solved the structure using XPREP and the SHELX[40] intrinsic phasing algorithm. While refining the structure with the SHELXL[41] least-squares algorithm in the program OLEX2,[42] we applied an extinction correction that improved the fit. The structure matched the known $P\bar{1}$ space group structure of $NbSe_2I_2$.[35] Powder X-ray diffraction (XRD) was performed on a Bruker D8 ADVANCE instrument using crushed crystals. The result was refined by GSAS-II[43] to verify the structure of $NbSe_2I_2$. Scanning electron microscopy (SEM) was performed on a ThermoFisher Axia ChemiSEM.

Exfoliation, Raman Spectroscopy, and Atomic Force Microscopy. The exfoliation of $NbSe_2I_2$ single crystals was carried out under ambient atmosphere. We used 3M Scotch tape to cleave a crystal around 10 times and exfoliated the flake onto a 285 nm/550 μm SiO_2/Si wafer (Nova Inc.). After exfoliation, the sample was kept in a N_2 glovebox until optical spectroscopy measurements. Raman spectroscopy was carried out in a Nanophoton Raman 11 spectrometer under an ambient atmosphere with a 532 nm laser and optical grating with 2400 lines per mm. The laser spot size was estimated to be 0.7 μm, with an intensity of 0.1 mW and a 10 s count time. After the raw spectra were obtained, a clean silicon wafer was used to calibrate the spectra with the characteristic Raman resonance peak of silicon at 520 cm^{-1}. Atomic force microscopy (AFM) was performed on an Oxford Instrument Cypher AFM setup. We used a standard AFM tip with reflective coating to do the imaging in the tapping mode, and the scan frequency was 0.8 Hz per line, with 512 lines per scan. The AFM image is shown in Figure S8,[39] which proves that the exfoliated crystal was monolayered.

Band Structure Calculation. The calculations of band structures using DFT were conducted with the VASP code.[44,45] We employed the VASP 5.4 PBE projector-augmented wave (PAW) pseudopotentials and the optB88-vdW functions[46] for band structure calculations. The total valence electrons explicitly treated in the DFT calculations consisted of Nb $4p^6 5s^1 4d^4$, Se $4s^2 4p^4$, and I $5s^2 5p^5$, which were described by a plane-wave basis set with a cutoff energy of 550 eV. We performed self-consistent calculations with spin−orbit coupling on the primitive $P\bar{1}$ structure, allowing atom position relaxation, using all-acute angles to be compatible with the standard k-path,[47] similar to the cell definition in the Open Quantum Materials Database:[48,49] a = 6.993 Å, b = 7.136 Å, c = 7.768 Å; $\alpha = 67.994°$, $\beta = 66.801°$, and $\gamma = 59.462°$. To simulate the monolayer structure, the vacuum spacing between the van der Waals layers was increased to 18 Å, and the input k-path of the two-dimensional 2D Brillouin zone for the single layer

https://doi.org/10.1021/acs.inorgchem.3c03493
Inorg. Chem. 2024, 63, 1119−1126

calculation was selected using the VASPKIT code[50] with the high symmetry points being: Γ (0, 0, 0), X (0.5, 0, 0), H1 (0.66, 0.32, 0), C (0.5, 0.5, 0), H (0.34, 0.68, 0), and Y (0, 0.5, 0).

Resistivity, Magnetic, and Thermal Measurements. An in-line, four-point resistivity measurement was carried out with a quantum design physical property measurement system (PPMS). A single crystal (about 2 × 2 × 0.1 mm) was chosen, and the contacts were made using gold wires and silver epoxy on the flat plane of the crystal. The crystal was approximately 2 mm wide and 0.1 mm thick with two inner voltage leads having a distance of about 0.5 mm.

Another $NbSe_2I_2$ single crystal (about 1 × 1 × 0.1 mm) was loaded into a quantum design magnetic property measurement system using a quartz holder. The applied magnetic field was in the flat plane of the crystal, and the moment was measured in vibrating sample magnetometry mode.

Differential scanning calorimetry (DSC) measurement was performed for a crystal weighing 2 mg on a TA Discovery 2500. The sample was ramped from 30 to −140 °C (the lowest temperature of the instrument) and then back to 30 °C. This process was repeated, and only the data for the second cycle were taken. To study the possible phase transformations at low temperatures, a crystal weighing 2 mg was loaded into the PPMS, and the heat capacity vs temperature curve was measured from 8 K (base temperature) to 145 K (−128 °C).

No uncommon hazards were noted.

RESULTS AND DISCUSSION

Crystal Structure of $NbSe_2I_2$. Figure 1 shows the optical and SEM images of the $NbSe_2I_2$ crystals. $NbSe_2I_2$ crystals have flat, dark (almost black) surfaces without a regular geometric shape or obvious faceting angles. The SEM image reveals that the crystals have terraced surfaces, which may indicate exfoliable layers, and angles near 120° can be seen on multiple facets of the crystal.

Single-crystal XRD was performed to unveil the crystallographic information on $NbSe_2I_2$, and the detailed information is listed in Table 1 in Supporting Information.[39] $NbSe_2I_2$ is triclinic at room temperature. It has a space group $P\bar{1}$ (no. 2), iso-structural to $NbSe_2Br_2$,[51] and this matches the previously published low-temperature (<199 °C) structure for $NbSe_2I_2$.[35]

Above the transition temperature at around 199 °C, a higher-symmetry monoclinic phase with a space group of $C2/m$ (no. 12) is more stable for $NbSe_2I_2$,[35] and it can be inferred that the $C2/m$ phase formed first during CVT growth and then transformed into the $P\bar{1}$ phase as the sample cooled naturally. The transformation from the $C2/m$ phase to the $P\bar{1}$ phase can be understood as a sliding of *ab*-plane sheets as well as a twist of atoms in the *ab*-plane.

Figure 2 shows the crystal structure of triclinic $NbSe_2I_2$, and Figure S2 in Supporting Information shows the crystal structure of the monoclinic $C2/m$ phase as a comparison.[39] In Figure 2a, it is obvious that the $NbSe_2I_2$ crystal has parallel *ab*-plane sheets bonded by van der Waals interactions. Figure 2b shows the *ab*-plane of triclinic $NbSe_2I_2$. Here, it can be seen that loops are formed in the *ab*-plane, which consists of 6 Nb^{4+} ions in total. The iodine ions are all bonded to niobium, and the Nb−I distance ranges from 2.9644 to 2.9764 Å. This distance range confirms the Nb−I bonding, which is seen in some but not all Nb−Se−I compounds.[29] Figure S3 in Supporting Information shows the visualization of the Nb−I distance comparison.[39]

All of the selenium ions are dimerized, forming Se_2^{2-} dimers between niobium ions. Given the fact that all iodine and selenium ions have a 1− valence, we know from charge counting that all the niobium ions have a valence of 4+, leaving one unpaired 4d electron for each Nb^{4+}. Looking closer at the *ab*-plane structure, it can be seen that the Nb−Nb distance through two Se_2^{2-} dimers (2.947(2) Å) is significantly shorter than the Nb−Nb distance through two I^- (4.725(2) or 4.697(2) Å), indicating that a Nb−Nb single bond is formed between the closer neighbors, leaving no free electrons.

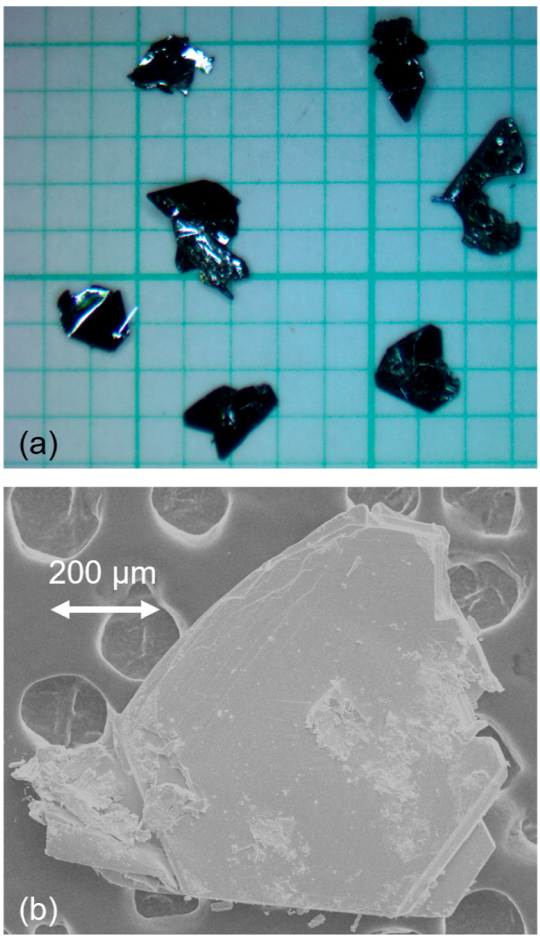

Figure 1. (a) Photograph of $NbSe_2I_2$ crystals obtained from CVT growth; the background is in millimeter scale. (b) SEM of a small $NbSe_2I_2$ crystal on carbon tape.

Considering the complicated triclinic crystal structure with very low symmetry and the balanced charge without free electrons for further modulation, especially one-dimensional modulation, CDW is not expected for triclinic $P\bar{1}$ $NbSe_2I_2$, unlike materials with intermediate $Ta^{4+/5+}$ or $Nb^{4+/5+}$ valences, such as $(TaSe_4)_2I$,[52] $(NbSe_4)_2I$,[53] and $(NbSe_4)_{3.33}I$.[20]

Figure 3 shows the Rietveld-refined powder XRD pattern for ground triclinic $NbSe_2I_2$ crystals, with R_w = 7.955%. The peak intensity is relatively low because limited crystals were ground, and strain was introduced during grinding. Overall, all the peaks are matched, and no impurity can be seen, and this verifies the structure determined from single-crystal XRD.

One interesting feature of the crystal structure is the *ab*-plane crystallographic angle γ = 61.3°, which can be seen from the unit cell in Figure 2b. This nonspecial number is, however, very close to 60°, thus making the crystals look very much like a hexagonal one with 120° angles, as shown in the bottom right part of the SEM image in Figure 1b. If $NbSe_2I_2$ crystals can be exfoliated and if the exfoliated crystals can maintain environmental stability, then they may be an excellent candidate for

https://doi.org/10.1021/acs.inorgchem.3c03493
Inorg. Chem. 2024, 63, 1119−1126

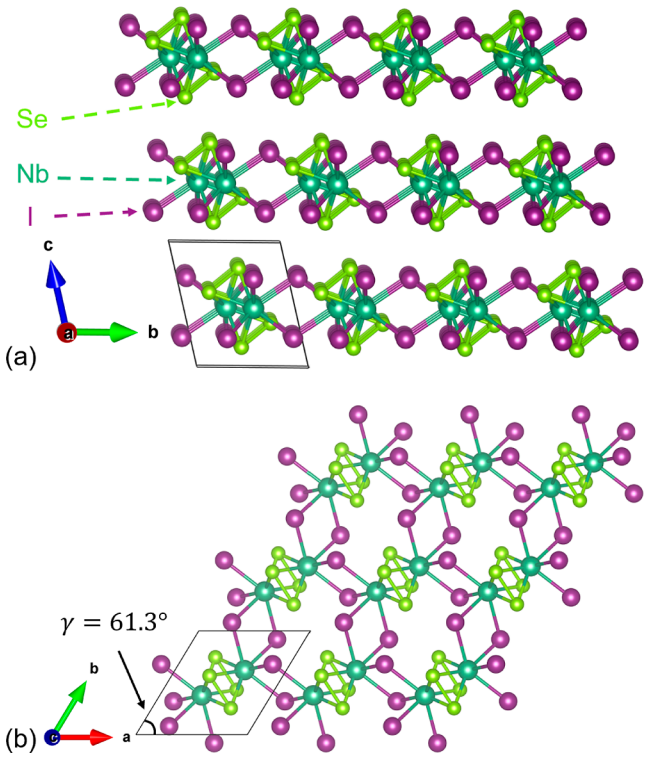

Figure 2. (a) Triclinic ($P\bar{1}$) $NbSe_2I_2$ crystal structure viewed along the *a*-axis (slightly tilted), showing the 2D planes in the *ab*-plane. (b) *ab*-plane of $NbSe_2I_2$, where loops form with 6 Nb^{4+} ions. In each loop, the Nb−Nb distance is shorter where there are 2 Se_2^{2-} dimers between them, while the Nb−Nb distance is longer when there are two iodine atoms in between. The unit cell is shown at the bottom left corner in both (a,b).

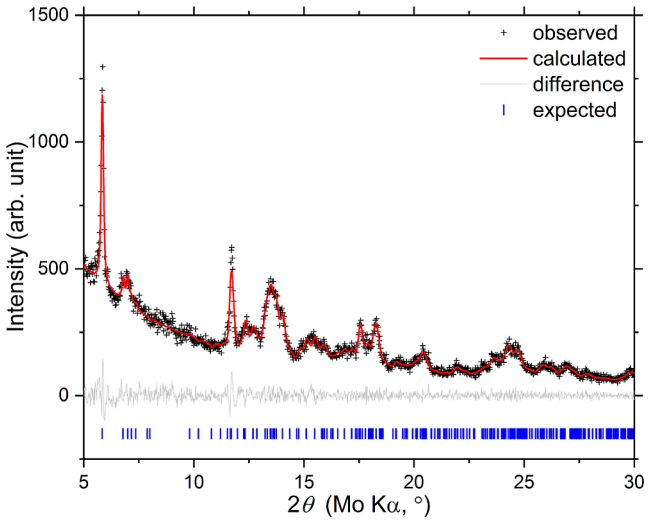

Figure 3. Rietveld refinement to the powder XRD pattern of $NbSe_2I_2$, with R_w = 7.955%.

the construction of Moiré superlattice heterostructures with hexagonal van der Waals materials.[54]

Exfoliation and Raman Spectroscopy of $NbSe_2I_2$. The triclinic $NbSe_2I_2$ has a van der Waals-layered structure, so it should be exfoliable down to few-layer flakes. We mechanically exfoliated $NbSe_2I_2$ single crystals with the established Scotch tape method onto a 285 nm-thick SiO_x on Si wafer and obtained flakes down to few-layer and monolayer thickness. Figure 4a shows optical microscopy images of the resulting exfoliated $NbSe_2I_2$. Due to thin film interferometry, the

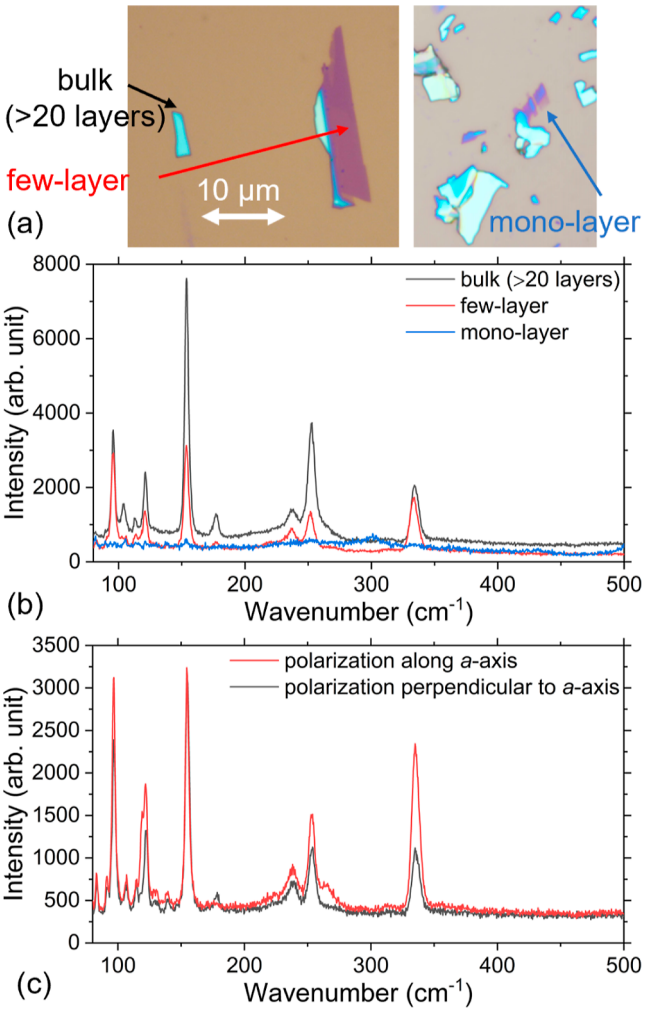

Figure 4. (a) Optical microscopic images of exfoliated triclinic $NbSe_2I_2$ crystals, showing bulk (more than 20 layers), few-layer, and monolayer structures. The 10 μm scale bar applies to both images. (b) Raman spectra of the exfoliated triclinic $NbSe_2I_2$ bulk, few-layer, and monolayer regions. (c) Polarized Raman spectroscopy on few-layer triclinic $NbSe_2I_2$, with incident light polarized along the *a*-axis or perpendicular to the *a*-axis. The two red curves in (b,c) are identical.

changes in color correspond with changes in the thickness of the film. SiO_x on the Si substrate is brown/tan (with different colors in the different images due to changes in illumination levels), the monolayer crystal appears as a light, translucent purple color, while the few-layer crystal has a darker, opaque purple color, and the bulk crystals are light blue. Raman spectroscopy probes the phonon transitions in 2D materials, making it a quick, nondestructive method to identify many structural and electronic properties such as the layer number,[55,56] lattice symmetry,[57,58] edge termination, strain,[59−63] doping,[61,62] defects,[64,65] and magnetic order.[66,67] Figure 4b shows the Raman spectra of the bulk (more than 20 layers), few-layer, and monolayer crystals. The Raman modes for the bulk and few-layer crystals match well, with only a difference in intensity, suggesting the preservation of the crystal structure and the electronic levels after exfoliation. In contrast, the Raman spectrum of the monolayer flake shows

https://doi.org/10.1021/acs.inorgchem.3c03493
Inorg. Chem. 2024, 63, 1119−1126

weak to no signal compared with that from thicker samples. We attribute this to two possible scenarios. First, many 2D van der Waals materials are reactive to air,[68,69] with the outer layers oxidizing, thus making monolayers unstable. Second, even if the crystal is stable, it may degrade due to thermal effects during the intense laser excitation of Raman spectroscopy.[70]

Next, in Figure 4c, we performed polarized Raman spectroscopy to probe the crystal structure. The two spectra show the response for excitation polarized along $\langle ZXX\bar{Z}\rangle$ and perpendicular to $\langle ZYY\bar{Z}\rangle$, with the horizontal X axis aligned to the long, cleaved edge of the few-layer sample in Figure 4. In particular, during exfoliation, van der Waals crystals tend to cleave along the low-symmetry axis,[57,58] which we assume to be oriented along the a-axis. The two spectra show that some of the Raman modes exist at both polarizations, while other modes exist only at one polarization. This behavior is similar to what is observed in other 2D materials with lower symmetry and can be used as a method for identifying lattice orientation.[58,71] Finally, in addition to Raman spectroscopy, photoluminescence (PL) spectroscopy was performed to probe the optical transitions. As shown in Figure S4,[40] there were no distinct peaks observed, suggesting that the material has an indirect band gap, which we show here subsequently.

Band Structure Calculations. To further study the electronic band structure of triclinic $NbSe_2I_2$, we employed the VASP 5.4 PBE PAW pseudopotentials and the optB88-vdW functions for band structure calculations for both bulk and monolayer structures, as shown in Figure 5. Figure 5a is for bulk triclinic $NbSe_2I_2$ and 5b is for monolayer triclinic $NbSe_2I_2$. Both bulk and monolayer triclinic $NbSe_2I_2$ are semiconductors, with an indirect band gap of 0.723 eV for bulk $NbSe_2I_2$ and 0.795 eV for monolayer $NbSe_2I_2$.

For both bulk and monolayer structures, there is an isolated band at around −0.5 eV, corresponding to the 4d band of niobium. The electronic band structures of bulk monoclinic ($C2/m$) $NbSe_2I_2$ were also calculated, as shown in Figure S5 in the Supporting Information, and the monoclinic and triclinic phases share the same general features.

Resistivity, Magnetic, and Thermal Properties of Bulk Triclinic $NbSe_2I_2$. A four-point resistivity measurement was performed on a bulk $NbSe_2I_2$ single crystal where the current was flowing in the ab-plane. Figure 6 shows both ρ versus T and ln (ρ) versus $1/T$ curves. The resistivity of $NbSe_2I_2$ increases on cooling, indicating semiconducting behavior. Noise in the resistivity measurement likely arises from the small sample size and the high resistance, near the maximum measurable for the instrument, which goes out of range below 200 K. The resistivity has a weak temperature dependence, which suggests a low activation energy, together with non-negligible intrinsic resistance from crystal defects.

For semiconductors, the Arrhenius equation $\rho = \rho_0 \exp\left(\frac{E_a}{k_B T}\right)$ holds. The straight blue line fits part of the ln (ρ) vs $1/T$ curve (red). From the slope of the blue line, the activation energy E_a was determined to be E_a = 5.4 meV. This is a very small number, much less than the PBE-DFT calculated at 1 eV. Once again, this may suggest the existence of defect electronic energy levels in the band gap. The difference in the activation energy with the theoretical band gap of our triclinic $NbSe_2I_2$ is larger than that of other van der Waals materials, such as MoS_2,[72] but it is also known that degradation can considerably lower the activation energy, as in the case of WTe_2.[73]

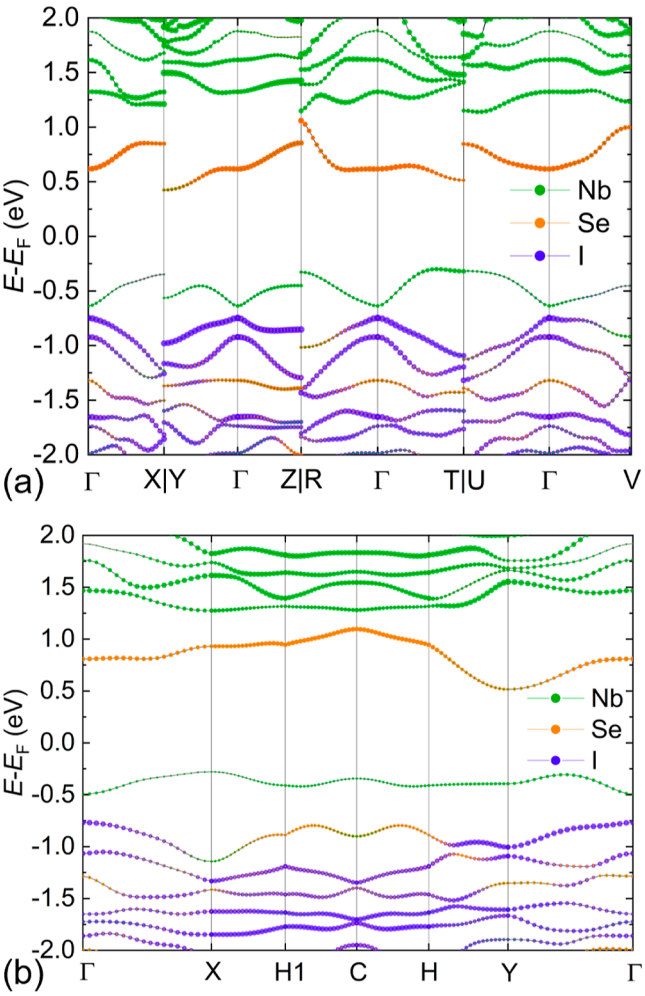

Figure 5. DFT-calculated band structures for (a) bulk $NbSe_2I_2$ and (b) monolayer $NbSe_2I_2$.

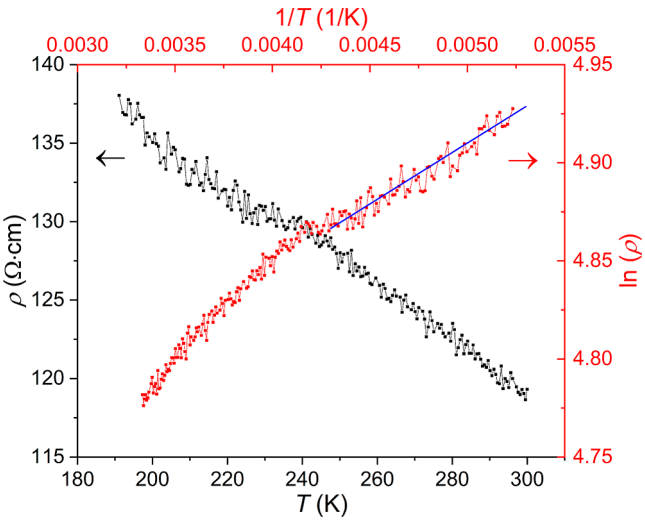

Figure 6. Four-point resistivity of a bulk $NbSe_2I_2$ crystal. The black and red dots and lines show ρ vs T and ln (ρ) vs $1/T$, respectively. The blue straight line fits part of the ln (ρ) vs $1/T$ curve to determine the Arrhenius activation energy E_a = 5.4 meV.

Thermal measurements below room temperature were also conducted, with DSC and PPMS heat capacities, with data shown in Figure S6,[39] and there were no phase transitions

https://doi.org/10.1021/acs.inorgchem.3c03493
Inorg. Chem. 2024, 63, 1119−1126

detected for $NbSe_2I_2$. Magnetic measurements verified that triclinic $NbSe_2I_2$ is indeed diamagnetic,[35] and the magnetization (M) vs field (H) curves are shown in Figure S7.

CONCLUSIONS

Single crystals of triclinic $NbSe_2I_2$ have been grown by a reliable two-tube CVT method that also produces quasi-one-dimensional $(Nb_4Se_{15}I_2)I_2$, and the $P\bar{1}$ crystal structure has been verified. The exfoliation of $NbSe_2I_2$ down to few-layer and monolayer structures was shown, and Raman spectroscopy was conducted on bulk, few-layer, and monolayer samples. Distinct Raman peaks are observed in the few-layer samples, while monolayers may suffer from beam damage or environmental degradation. Polarized Raman spectroscopy showed different transitions for different orientations, corresponding with the lattice symmetry of the crystal. $NbSe_2I_2$ is a semiconductor, which has been shown by PBE-DFT calculations as well as resistivity measurements. It does not undergo phase transformations below room temperature, and it stays as a diamagnet. It remains to be seen whether strain can be a factor to alter the electronic structure of $NbSe_2I_2$ or to change the transition temperature between the triclinic and monoclinic phases. Furthermore, thin-film heterostructures are also possibilities to tune the property of $NbSe_2I_2$ or to utilize $NbSe_2I_2$ as a medium to introduce strain due to its triclinic to monoclinic structural transition at around 200 °C. Moreover, the in-plane angle $\gamma = 61.3°$ would make $NbSe_2I_2$ an incredible substrate to tune other hexagonal van der Waals materials by introducing strain and to potentially alter their electronic properties by introducing Moiré superlattice.

ASSOCIATED CONTENT

Supporting Information

The Supporting Information is available free of charge at https://pubs.acs.org/doi/10.1021/acs.inorgchem.3c03493.

> Photos of CVT reaction tubes, detailed crystallographic information on triclinic $NbSe_2I_2$, crystal structure of monoclinic $NbSe_2I_2$, Nb−I distance comparison, PL measurement of the triclinic $NbSe_2I_2$ bulk crystal, DFT band calculations of bulk monoclinic $NbSe_2I_2$, DSC and PPMS heat capacity measurement results of triclinic $NbSe_2I_2$, magnetization (M) vs field (H) measurement result of triclinic $NbSe_2I_2$, and AFM image of exfoliated $NbSe_2I_2$ (PDF)

Accession Codes

CCDC 2312751 contains the supplementary crystallographic data for this paper. These data can be obtained free of charge via www.ccdc.cam.ac.uk/data_request/cif, or by emailing data_request@ccdc.cam.ac.uk, or by contacting The Cambridge Crystallographic Data Centre, 12 Union Road, Cambridge CB2 1EZ, UK; fax: +44 1223 336033.

AUTHOR INFORMATION

Corresponding Author

Daniel P. Shoemaker − *Department of Materials Science and Engineering and Materials Research Laboratory, University of Illinois at Urbana-Champaign, Urbana, Illinois 61801, United States;* orcid.org/0000-0003-3650-7551; Email: dpshoema@illinois.edu

Authors

Kejian Qu − *Department of Physics, University of Illinois at Urbana-Champaign, Urbana, Illinois 61801, United States; Materials Research Laboratory, University of Illinois at Urbana-Champaign, Urbana, Illinois 61801, United States;* orcid.org/0000-0002-7189-537X

Yue Zhang − *Department of Mechanical Science and Engineering, University of Illinois at Urbana-Champaign, Urbana, Illinois 61801, United States;* orcid.org/0000-0002-3087-6965

Cheng Peng − *Stanford Institute for Materials and Energy Sciences, SLAC National Accelerator Laboratory, Menlo Park, California 94025, United States*

Zachary W. Riedel − *Department of Materials Science and Engineering and Materials Research Laboratory, University of Illinois at Urbana-Champaign, Urbana, Illinois 61801, United States;* orcid.org/0000-0001-5848-5520

Juyeon Won − *Department of Materials Science and Engineering and Materials Research Laboratory, University of Illinois at Urbana-Champaign, Urbana, Illinois 61801, United States*

Rong Zhang − *Stanford Institute for Materials and Energy Sciences, SLAC National Accelerator Laboratory, Menlo Park, California 94025, United States; Department of Applied Physics, Stanford University, Stanford, California 94305, United States*

Toby J. Woods − *George L. Clark X-Ray Facility and 3M Materials Laboratory, University of Illinois at Urbana-Champaign, Urbana, Illinois 61801, United States;* orcid.org/0000-0002-1737-811X

Tom Devereaux − *Stanford Institute for Materials and Energy Sciences, SLAC National Accelerator Laboratory, Menlo Park, California 94025, United States; Department of Materials Science and Engineering, Stanford University, Stanford, California 94305, United States*

Arend M. van der Zande − *Department of Mechanical Science and Engineering and Materials Research Laboratory, University of Illinois at Urbana-Champaign, Urbana, Illinois 61801, United States;* orcid.org/0000-0001-5104-9646

Complete contact information is available at: https://pubs.acs.org/10.1021/acs.inorgchem.3c03493

Notes

The authors declare no competing financial interest.

ACKNOWLEDGMENTS

Crystal growth, transport, microstructure characterization, and computation were supported by the Center for Quantum Sensing and Quantum Materials, an Energy Frontier Research Center funded by the U.S. Department of Energy, Office of Science, Basic Energy Sciences, under award no. DE-SC0021238. Exfoliation and Raman characterization were supported by an NSF-MRSEC award no. DMR-1720633 and an NSF-CAREER award no. CMMI-184673. The authors acknowledge the use of microscopy facilities at the Materials Research Laboratory Central Research Facilities, University of Illinois, and the use of facilities and instrumentation supported by NSF through the University of Illinois Materials Research Science and Engineering Center DMR-1720633. Cheng Peng acknowledges the support of the U.S. Department of Energy, Office of Science, Basic Energy Sciences, under award no. DE-SC0022216.

REFERENCES

(1) Novoselov, K. S.; Geim, A. K.; Morozov, S. V.; Jiang, D.; Zhang, Y.; Dubonos, S. V.; Grigorieva, I. V.; Firsov, A. A. Electric Field Effect in Atomically Thin Carbon Films. *Science* **2004**, *306*, 666−669.

(2) Randviir, E. P.; Brownson, D. A.; Banks, C. E. A decade of graphene research: production, applications and outlook. *Mater. Today* **2014**, *17*, 426−432.

(3) Ares, P.; Novoselov, K. S. Recent advances in graphene and other 2D materials. *Nano Mater. Sci.* **2022**, *4*, 3−9.

(4) Tang, Q.; Zhou, Z.; Chen, Z. Innovation and discovery of graphene-like materials via density-functional theory computations. *Wiley Interdiscip. Rev.: Comput. Mol. Sci.* **2015**, *5* (5), 360−379.

(5) Kheirabadi, N.; Shafiekhani, A.; Fathipour, M. Review on graphene spintronic, new land for discovery. *Superlattices Microstruct.* **2014**, *74*, 123−145.

(6) Craciun, M.; Russo, S.; Yamamoto, M.; Tarucha, S. Tuneable electronic properties in graphene. *Nano Today* **2011**, *6*, 42−60.

(7) Golberg, D.; Bando, Y.; Huang, Y.; Terao, T.; Mitome, M.; Tang, C.; Zhi, C. Boron Nitride Nanotubes and Nanosheets. *ACS Nano* **2010**, *4*, 2979−2993.

(8) Wang, J.; Xu, X.; Mu, X.; Ma, F.; Sun, M. Magnetics and spintronics on two-dimensional composite materials of graphene/hexagonal boron nitride. *Mater. Today Phys.* **2017**, *3*, 93−117.

(9) Manzeli, S.; Ovchinnikov, D.; Pasquier, D.; Yazyev, O. V.; Kis, A. 2D transition metal dichalcogenides. *Nat. Rev. Mater.* **2017**, *2*, 17033.

(10) Voiry, D.; Mohite, A.; Chhowalla, M. Phase engineering of transition metal dichalcogenides. *Chem. Soc. Rev.* **2015**, *44*, 2702−2712.

(11) Krishnan, U.; Kaur, M.; Singh, K.; Kumar, M.; Kumar, A. A synoptic review of MoS_2: Synthesis to applications. *Superlattices Microstruct.* **2019**, *128*, 274−297.

(12) Tian, W.; Yu, W.; Liu, X.; Wang, Y.; Shi, J. A Review of the Characteristics, Synthesis, and Thermodynamics of Type-II Weyl Semimetal WTe_2. *Materials* **2018**, *11*, 1185.

(13) Peng, L.; Yuan, Y.; Li, G.; Yang, X.; Xian, J.-J.; Yi, C.-J.; Shi, Y.-G.; Fu, Y.-S. Observation of topological states residing at step edges of WTe_2. *Nat. Commun.* **2017**, *8*, 659.

(14) Samal, R.; Sanyal, G.; Chakraborty, B.; Rout, C. S. Two-dimensional transition metal phosphorous trichalcogenides (MPX3): a review on emerging trends, current state and future perspectives. *J. Mater. Chem. A* **2021**, *9*, 2560−2591.

(15) Le Flem, G.; Brec, R.; Ouvard, G.; Louisy, A.; Segransan, P. Magnetic interactions in the layer compounds MPX_3 (M = Mn, Fe, Ni; X = S, Se). *J. Phys. Chem. Solids* **1982**, *43*, 455−461.

(16) Bhutani, A.; Zuo, J. L.; McAuliffe, R. D.; dela Cruz, C. R.; Shoemaker, D. P. Strong anisotropy in the mixed antiferromagnetic system $Mn_{1-x}Fe_xPSe_3$. *Phys. Rev. Mater.* **2020**, *4*, 034411.

(17) Fedorov, V. E.; Mishchenko, A. V.; Fedin, V. P. Cluster Transition Metal Chalcogenide Halides. *Russ. Chem. Rev.* **1985**, *54*, 408−423.

(18) Kim, S.; Lv, Y.; Sun, X.-Q.; Zhao, C.; Bielinski, N.; Murzabekova, A.; Qu, K.; Duncan, R. A.; Nguyen, Q. L. D.; Trigo, M.; Shoemaker, D. P.; Bradlyn, B.; Mahmood, F. Observation of a massive phason in a charge-density-wave insulator. *Nat. Mater.* **2023**, *22*, 429−433.

(19) Nguyen, Q. L.; Duncan, R. A.; Orenstein, G.; Huang, Y.; Krapivin, V.; de la Peña, G.; Ornelas-Skarin, C.; Reis, D. A.; Abbamonte, P.; Bettler, S.; Chollet, M.; Hoffmann, M. C.; Hurley, M.; Kim, S.; Kirchmann, P. S.; Kubota, Y.; Mahmood, F.; Miller, A.; Osaka, T.; Qu, K.; Sato, T.; Shoemaker, D. P.; Sirica, N.; Song, S.; Stanton, J.; Teitelbaum, S. W.; Tilton, S. E.; Togashi, T.; Zhu, D.; Trigo, M. Ultrafast X-Ray Scattering Reveals Composite Amplitude Collective Mode in the Weyl Charge Density Wave Material $(TaSe_4)_2I$. *Phys. Rev. Lett.* **2023**, *131*, 076901.

(20) Wang, Z. Z.; Monceau, P.; Renard, M.; Gressier, P.; Guemas, L.; Meerschaut, A. Charge density transport in a novel halogened transition metal tetrachalcogenide $(NbSe_4)_{3.33}I$. *Solid State Commun.* **1983**, *47*, 439−443.

(21) Hossain, M.; Qin, B.; Li, B.; Duan, X. Synthesis, characterization, properties and applications of two-dimensional magnetic materials. *Nano Today* **2022**, *42*, 101338.

(22) Sasaki, K.; Uchida, Y.; Nishiyama, N. Bottom-up Synthesis of Nanosheets at Various Interfaces. *ChemPlusChem* **2023**, *88* (10), No. e202300255.

(23) Zhang, Y.; Zhang, L.; Zhou, C. Review of Chemical Vapor Deposition of Graphene and Related Applications. *Acc. Chem. Res.* **2013**, *46*, 2329−2339.

(24) Joyce, B. A. Molecular beam epitaxy. *Rep. Prog. Phys.* **1985**, *48*, 1637−1697.

(25) Wang, D.; Luo, F.; Lu, M.; Xie, X.; Huang, L.; Huang, W. Chemical Vapor Transport Reactions for Synthesizing Layered Materials and Their 2D Counterparts. *Small* **2019**, *15*, 1804404.

(26) Zhu, X.; Ling, L.; Han, Y.; Xu, J.; Wang, Y.; Zhang, H.; Zhang, C.; Pi, L.; Zhang, Y. Single crystal growth of the new pressure-induced-superconductor CrAs via chemical vapor transport. *J. Alloys Compd.* **2016**, *677*, 57−60.

(27) Ubaldini, A.; Jacimovic, J.; Ubrig, N.; Giannini, E. Chloride-Driven Chemical Vapor Transport Method for Crystal Growth of Transition Metal Dichalcogenides. *Cryst. Growth Des.* **2013**, *13*, 4453−4459.

(28) Binnewies, M.; Schmidt, M.; Schmidt, P. Chemical Vapor Transport Reactions − Arguments for Choosing a Suitable Transport Agent. *Z. Anorg. Allg. Chem.* **2017**, *643*, 1295−1311.

(29) Qu, K.; Riedel, Z. W.; Sánchez-Ramírez, I.; Bettler, S.; Oh, J.; Waite, E. N.; Woods, T. J.; Mason, N.; Abbamonte, P.; de Juan, F.; Vergniory, M. G.; Shoemaker, D. P. Quasi-One-Dimensional Transition-Metal Chalcogenide Semiconductor $(Nb_4Se_{15}I_2)I_2$. *Inorg. Chem.* **2023**, *62*, 3067−3074.

(30) Cao, Y.; Fatemi, V.; Demir, A.; Fang, S.; Tomarken, S. L.; Luo, J. Y.; Sanchez-Yamagishi, J. D.; Watanabe, K.; Taniguchi, T.; Kaxiras, E.; Ashoori, R. C.; Jarillo-Herrero, P. Correlated insulator behaviour at half-filling in magic-angle graphene superlattices. *Nature* **2018**, *556*, 80−84.

(31) Cao, Y.; Fatemi, V.; Fang, S.; Watanabe, K.; Taniguchi, T.; Kaxiras, E.; Jarillo-Herrero, P. Unconventional superconductivity in magic-angle graphene superlattices. *Nature* **2018**, *556*, 43−50.

(32) Ponomarenko, L. A.; Gorbachev, R. V.; Yu, G. L.; Elias, D. C.; Jalil, R.; Patel, A. A.; Mishchenko, A.; Mayorov, A. S.; Woods, C. R.; Wallbank, J. R.; Mucha-Kruczynski, M.; Piot, B. A.; Potemski, M.; Grigorieva, I. V.; Novoselov, K. S.; Guinea, F.; Fal'ko, V. I.; Geim, A. K. Cloning of Dirac fermions in graphene superlattices. *Nature* **2013**, *497*, 594−597.

(33) Dean, C. R.; Wang, L.; Maher, P.; Forsythe, C.; Ghahari, F.; Gao, Y.; Katoch, J.; Ishigami, M.; Moon, P.; Koshino, M.; Taniguchi, T.; Watanabe, K.; Shepard, K. L.; Hone, J.; Kim, P. Hofstadter's butterfly and the fractal quantum Hall effect in moiré superlattices. *Nature* **2013**, *497*, 598−602.

(34) Hunt, B.; Sanchez-Yamagishi, J. D.; Young, A. F.; Yankowitz, M.; LeRoy, B. J.; Watanabe, K.; Taniguchi, T.; Moon, P.; Koshino, M.; Jarillo-Herrero, P.; Ashoori, R. C. Massive Dirac Fermions and Hofstadter Butterfly in a van der Waals Heterostructure. *Science* **2013**, *340*, 1427−1430.

(35) Miller, G. J. Chemistry and properties of novel niobium cluster compounds. *J. Alloys Compd.* **1995**, *229*, 93−106.

(36) Weissenstein, J.; Horák, J. Preparation and some physical properties of $NbSe_2I_2$ crystals. *Czech. J. Phys. B* **1974**, *24*, 235−238.

(37) Rijnsdorp, J.; de Lange, G.; Wiegers, G. Preparation, structures, and properties of niobium chalcogenide halides, NbX_2Y_2 (X = S, Se; Y = Cl, Br, I). *J. Solid State Chem.* **1979**, *30*, 365−373.

(38) Maki, M.; Kaiser, M.; Zettl, A.; Grüner, G. Charge density wave transport in a novel inorganic chain compound, $(TaSe_4)_2I$. *Solid State Commun.* **1983**, *46*, 497−500.

(39) See Supporting Information.

(40) Sheldrick, G. M. A short history of *SHELX*. *Acta Crystallogr., Sect. A* **2008**, *64*, 112−122.

(41) Sheldrick, G. M. Crystal structure refinement with *SHELXL*. *Acta Crystallogr., Sect. C: Struct. Chem.* **2015**, *71*, 3−8.

https://doi.org/10.1021/acs.inorgchem.3c03493
Inorg. Chem. 2024, 63, 1119−1126

(42) Dolomanov, O. V.; Bourhis, L. J.; Gildea, R. J.; Howard, J. A. K.; Puschmann, H. *OLEX2*: a complete structure solution, refinement and analysis program. *J. Appl. Crystallogr.* **2009**, *42*, 339−341.
(43) Toby, B. H.; Von Dreele, R. B. *GSAS-II*: the genesis of a modern open-source all purpose crystallography software package. *J. Appl. Crystallogr.* **2013**, *46*, 544−549.
(44) Kresse, G.; Hafner, J. Ab initio molecular dynamics for open-shell transition metals. *Phys. Rev. B* **1993**, *48*, 13115−13118.
(45) Kresse, G.; Hafner, J. Ab initio molecular-dynamics simulation of the liquid-metal−amorphous-semiconductor transition in germanium. *Phys. Rev. B* **1994**, *49*, 14251−14269.
(46) Klimeš, J.; Bowler, D. R.; Michaelides, A. Chemical accuracy for the van der Waals density functional. *J. Phys.: Condens. Matter* **2010**, *22*, 022201.
(47) Hinuma, Y.; Pizzi, G.; Kumagai, Y.; Oba, F.; Tanaka, I. Band structure diagram paths based on crystallography. *Comput. Mater. Sci.* **2017**, *128*, 140−184.
(48) Saal, J. E.; Kirklin, S.; Aykol, M.; Meredig, B.; Wolverton, C. Materials Design and Discovery with High-Throughput Density Functional Theory: The Open Quantum Materials Database (OQMD). *JOM* **2013**, *65*, 1501−1509.
(49) Kirklin, S.; Saal, J. E.; Meredig, B.; Thompson, A.; Doak, J. W.; Aykol, M.; Rühl, S.; Wolverton, C. The Open Quantum Materials Database (OQMD): assessing the accuracy of DFT formation energies. *npj Comput. Mater.* **2015**, *1* (1), 15010.
(50) Wang, V.; Xu, N.; Liu, J.-C.; Tang, G.; Geng, W.-T. VASPKIT: A user-friendly interface facilitating high-throughput computing and analysis using VASP code. *Comput. Phys. Commun.* **2021**, *267*, 108033.
(51) Grenouilleau, P.; Meerschaut, A. $NbSe_2Br_2$: étude cristallographique des phases basse température et haute température. *Eur. J. Solid State Inorg. Chem.* **1988**, *25* (1), 77−89.
(52) Wang, Z. Z.; Saint-Lager, M. C.; Monceau, P.; Renard, M.; Gressier, P.; Meerschaut, A.; Guemas, L.; Rouxel, J. Charge density wave transport in $(TaSe_4)_2I$. *Solid State Commun.* **1983**, *46*, 325−328.
(53) Philipp, A.; Mayr, W.; Kim, T. W.; Alavi, B.; Maki, M.; Grüner, G. Dynamics of the charge-density-wave mode in $(NbSe_4)_2I$. *Phys. Rev. B* **1989**, *39*, 7536−7544.
(54) He, F.; Zhou, Y.; Ye, Z.; Cho, S.-H.; Jeong, J.; Meng, X.; Wang, Y. Moiré Patterns in 2D Materials: A Review. *ACS Nano* **2021**, *15*, 5944−5958.
(55) Lee, C.; Yan, H.; Brus, L. E.; Heinz, T. F.; Hone, J.; Ryu, S. Anomalous Lattice Vibrations of Single- and Few-Layer MoS_2. *ACS Nano* **2010**, *4*, 2695−2700.
(56) Ferrari, A. C.; Meyer, J. C.; Scardaci, V.; Casiraghi, C.; Lazzeri, M.; Mauri, F.; Piscanec, S.; Jiang, D.; Novoselov, K. S.; Roth, S.; Geim, A. K. Raman Spectrum of Graphene and Graphene Layers. *Phys. Rev. Lett.* **2006**, *97*, 187401.
(57) Guo, Y.; Liu, C.; Yin, Q.; Wei, C.; Lin, S.; Hoffman, T. B.; Zhao, Y.; Edgar, J. H.; Chen, Q.; Lau, S. P.; Dai, J.; Yao, H.; Wong, H.-S. P.; Chai, Y. Distinctive in-Plane Cleavage Behaviors of Two-Dimensional Layered Materials. *ACS Nano* **2016**, *10*, 8980−8988.
(58) Chenet, D. A.; Aslan, B.; Huang, P. Y.; Fan, C.; Van Der Zande, A. M.; Heinz, T. F.; Hone, J. C. In-plane anisotropy in mono-and few-layer ReS_2 probed by Raman spectroscopy and scanning transmission electron microscopy. *Nano Lett.* **2015**, *15*, 5667−5672.
(59) Huang, M.; Yan, H.; Heinz, T. F.; Hone, J. Probing strain-induced electronic structure change in graphene by Raman spectroscopy. *Nano Lett.* **2010**, *10* (10), 4074−4079.
(60) Yang, L.; Cui, X.; Zhang, J.; Wang, K.; Shen, M.; Zeng, S.; Dayeh, S. A.; Feng, L.; Xiang, B. Lattice strain effects on the optical properties of MoS_2 nanosheets. *Sci. Rep.* **2014**, *4*, 5649.
(61) Lee, J. E.; Ahn, G.; Shim, J.; Lee, Y. S.; Ryu, S. Optical separation of mechanical strain from charge doping in graphene. *Nat. Commun.* **2012**, *3*, 1024.
(62) Michail, A.; Delikoukos, N.; Parthenios, J.; Galiotis, C.; Papagelis, K. Optical detection of strain and doping inhomogeneities in single layer MoS_2. *Appl. Phys. Lett.* **2016**, *108*, 173102.
(63) Casiraghi, C.; Hartschuh, A.; Qian, H.; Piscanec, S.; Georgi, C.; Fasoli, A.; Novoselov, K. S.; Basko, D. M.; Ferrari, A. C. Raman Spectroscopy of Graphene Edges. *Nano Lett.* **2009**, *9*, 1433−1441.
(64) Eckmann, A.; Felten, A.; Mishchenko, A.; Britnell, L.; Krupke, R.; Novoselov, K. S.; Casiraghi, C. Probing the nature of defects in graphene by Raman spectroscopy. *Nano Lett.* **2012**, *12*, 3925−3930.
(65) Cançado, L. G.; Jorio, A.; Ferreira, E. H. M.; Stavale, F.; Achete, C. A.; Capaz, R. B.; Moutinho, M. V. O.; Lombardo, A.; Kulmala, T. S.; Ferrari, A. C. Quantifying Defects in Graphene via Raman Spectroscopy at Different Excitation Energies. *Nano Lett.* **2011**, *11*, 3190−3196.
(66) Wang, X.; Du, K.; Fredrik Liu, Y. Y.; Hu, P.; Zhang, J.; Zhang, Q.; Owen, M. H. S.; Lu, X.; Gan, C. K.; Sengupta, P.; Kloc, C.; Xiong, Q. Raman spectroscopy of atomically thin two-dimensional magnetic iron phosphorus trisulfide $FePS_3$ crystals. *2D Mater.* **2016**, *3* (3), 031009.
(67) Lee, J.-U.; Lee, S.; Ryoo, J. H.; Kang, S.; Kim, T. Y.; Kim, P.; Park, C.-H.; Park, J.-G.; Cheong, H. Ising-type magnetic ordering in atomically thin $FePS_3$. *Nano Lett.* **2016**, *16*, 7433−7438.
(68) Zhang, W.; Wong, P. K. J.; Zhu, R.; Wee, A. T. Van der Waals magnets: wonder building blocks for two-dimensional spintronics? *InfoMat* **2019**, *1*, 479−495.
(69) Gong, C.; Li, L.; Li, Z.; Ji, H.; Stern, A.; Xia, Y.; Cao, T.; Bao, W.; Wang, C.; Wang, Y.; Qiu, Z. Q.; Cava, R. J.; Louie, S. G.; Xia, J.; Zhang, X. Discovery of intrinsic ferromagnetism in two-dimensional van der Waals crystals. *Nature* **2017**, *546*, 265−269.
(70) Castellanos-Gomez, A.; Barkelid, M.; Goossens, A.; Calado, V. E.; van der Zant, H. S.; Steele, G. A. Laser-thinning of MoS_2: on demand generation of a single-layer semiconductor. *Nano Lett.* **2012**, *12*, 3187−3192.
(71) Wu, J.; Mao, N.; Xie, L.; Xu, H.; Zhang, J. Identifying the crystalline orientation of black phosphorus using angle-resolved polarized Raman spectroscopy. *Angew. Chem., Int. Ed.* **2015**, *54*, 2366−2369.
(72) El Beqqali, O.; Zorkani, I.; Rogemond, F.; Chermette, H.; Chaabane, R. B.; Gamoudi, M.; Guillaud, G. Electrical properties of molybdenum disulfide MoS_2. Experimental study and density functional calculation results. *Synth. Met.* **1997**, *90*, 165−172 Molecular Materials Applications to Sensors and Optoelectric Devices.
(73) Ye, F.; Lee, J.; Hu, J.; Mao, Z.; Wei, J.; Feng, P. X.-L. Environmental Instability and Degradation of Single- and Few-Layer WTe_2 Nanosheets in Ambient Conditions. *Small* **2016**, *12*, 5802−5808.

https://doi.org/10.1021/acs.inorgchem.3c03493
Inorg. Chem. 2024, 63, 1119−1126